Efficient Nonlinear Mass-Spring Model for Anatomical Virtual Reality

Wen Xu, Yong Wang, Weimin Huang, and Yuping Duan*

***Abstract*—The visuo-haptic surgical simulator providing both visual feedback and haptic interaction is very important for various applications such as surgical simulation, training, and planning. In this paper, we develop a nonlinear mass-spring model by introducing the elastica springs, which measure the soft tissue deformation based on both spring length and curvature. As a result, our model works well on the triangular surface meshes by producing more realistic simulations with smoother and plumper surfaces. Numerical experiments are conducted on both synthetic sphere and human liver models to demonstrate the superior performance of our method with both position-based and force-based interaction. Compared to the traditional and constrained mass-spring models, our model can well balance the accuracy and efficiency, providing simulation results with biomechanical properties such as nonlinearity and incompressibility. Furthermore, we implement the proposed model as the physical engine for a prototype of anatomical virtual reality, where realistic deformation is rendered at a refresh rate of 33 frames/s on a regular personal computer.**

***Index Terms*—Visuo-haptic surgical simulator, nonlinear mass-spring model, elastica spring, soft tissue modeling, anatomical virtual reality**

I. Introduction

THE visuo-haptic surgical simulator [1]–[5] is a kind of medical instruments, which exploits haptic technology to simulate the surgical procedure in a virtual way. A typical surgical simulator includes the force feedback system as input and output, and a computer to simulate the surgical procedure on virtual organs. Therefore, the users can see and touch the soft tissues via the visuo-haptic surgical simulator. As demonstrated in Fig. 1 (a), the users can operate a virtual scalpel on a virtual liver through the force feedback device, and the deformation of the liver as well as the feedback force on the scalpel are simulated by a mathematical model for the organ accurately and timely. Such an instrument has been increasingly used in surgical training [6]–[8], surgical planning [8]–[10], and rehabilitation [11]–[14].

One key component of such a surgical simulator is to develop a realistic soft tissue model providing both visual feedback and haptic interaction [15]–[17], as shown in Fig. 1 (b). Although numerous efforts have been devoted to the modeling of soft tissue deformation, it is still challenging to efficiently simulate the biological behaviors of soft tissues such as nonlinearity, viscoelasticity, anisotropy, and incompressibility, etc. A survey of the state-of-the-art deformable models for surgical simulators can be found in [18] and the references therein, which can be classified into two main categories: the continuum mechanical methodologies and discrete modeling methodologies. The first category employs the constitutive laws to model the elastic behavior of soft tissues, which requires to use the finite element method to solve the partial differential equations [17], [19], [20]. The representative of the second category is the mass-spring models (MSM), which describe the soft tissue as a network of point masses connected by the springs [21], [22]. Etzmuss *et al.* [23] further established the link between mass-spring systems and continuum mechanics by deriving a particle system from a continuum model using the finite difference method, which can approximate the continuous model with a high resolution. Besides, the hybrid soft tissue deformable models have been also proposed [15], [24].

The mass-spring model is a popular physics-based model for soft tissue simulation due to its simple mathematical formulation, high friendliness for topological changes, and low computational costs. When the external force is applied to the soft tissue, the deformation is characterized by the length deformation of the springs, which follows Hooke's law with a linear relationship between the stress and the resulting strain. Historically, Miller [25] has used the MSM to animate the motion dynamics of snakes and worms, which was further studied for surgical simulation [26], [27]. Later on, Teschner *et al.* [28] presented a fast tetrahedral mass-spring system to calculate soft tissue deformation caused by bone displacement in a short time interval. However, due to the use of the linear springs, the aforementioned MSMs failed to model the mechanical properties of soft tissues. Thus, many attempts have been made to improve the mass-spring system by either introducing additional nonlinear springs or artificial constraints on springs. For example, Nedel and Thalmann [29] proposed a mass-spring system with angular springs to control the volume of muscles during the simulation process. Hong *et al.* [30] used a volume-preserving constraint to guarantee the surface MSM can well approximate the linear FEM-based simulation. Basafa and Farahmand [31] introduced nonlinear springs and dampers into the mass-spring system to model the nonlinear and viscoelastic material properties in real-time. Xu *et al.* [32] proposed to incorporate viscoelasticity into

The work was partially supported by the Major Science and Technology Project of Tianjin 18ZXRHSY00160, National Natural Science Foundation of China (NSFC 12071345, 11701418), and the Recruitment Program of Global Young Expert. *Asterisk indicates the corresponding author.*

W. Xu is with the Center for Applied Mathematics, Tianjin University, Tianjin 300072, China.

Y. Wang is with School of Physics, Nankai University, Tianjin 300071, China.

W. Huang is with Institute for Infocomm Research, A*STAR, Singapore 138632, Singapore.

*Y. Duan is with the Center for Applied Mathematics, Tianjin University, Tianjin, China 300072. E-mail: yuping.duan@tju.edu.cn.

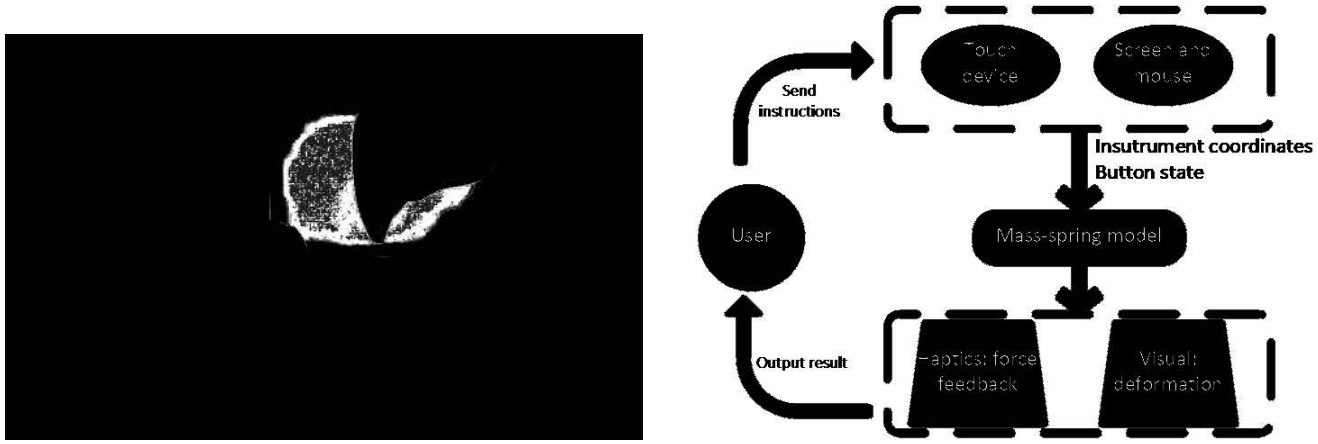

(a) (b)

Fig. 1. The configuration of our visuo-haptic simulator. (a) The photo of our visuo-haptic surgical simulator, which consists of a force feedback system and a personal computer; (b) the workflow of our visuo-haptic surgical simulator. The user can send instructions into the computer through the feedback force device, which is processed by our nonlinear mass-spring model and the computational algorithm. The output of the computer is transferred to the force feedback system, which is felt by the user.

the tensor-mass model for soft tissue. Gaizka *et al.* [33] developed a cubical mass-spring model consisting of edge springs, face diagonal springs, and internal diagonal springs to obtain realistic mechanical behavior of soft tissues. Duan *et al.* [22] proposed a tetrahedral MSM by introducing constraints on positions, which can preserve volume for realistic simulation of the incompressible tissues. Li *et al.* [34] developed a surface MSM with new flexion springs and a collision detection algorithm for achieving real-time performance. Golec *et al.* [24] suggested supplementing the spring deformation energy with volume-dependent energy to simulate any real isotropic materials.

Considering that the artificial springs and constraints lead to a significant increase in computational costs, we define the spring force with the elastica springs modeled by both spring length and spring curvature. Accordingly, we establish a nonlinear mass-spring model working as the physical engine for surgical simulators, which can not only estimate the realistic deformation of soft tissue but also provide the real-time interaction between the user and instrument. In particular, the distortion mechanism estimated by our MSM is non-linearly related to the external forces. More importantly, the elastica springs also promote the spring forces to be transferred from vertices of large curvatures to vertices of small curvatures to obtain smoother and plumper surfaces. Numerical experiments on both synthetic sphere model and real liver model show that the proposed MSM can well balance the computational efficiency and simulation accuracy under external loadings. Moreover, we demonstrate an interactive anatomical virtual reality equipped with the proposed MSM, which can provide a relatively high degree of realistic visual feedback at a refreshment rate of 33 frames/s on a regular PC.

The rest of the paper is organized as follows. In Section II, we describe our nonlinear mass-spring model and the computational algorithm in detail. In Section III, the advantageous performance of our model is validated by comparing with the traditional MSM and constrained MSM [22] on both synthetic sphere and human liver models. In Section IV, we further apply the proposed model to realize an anatomical virtual reality system. A brief discussion and the concluding remarks are presented in Section V.

II. The Nonlinear mass-spring model

A. Preliminaries

In this section, we introduce basic notations of triangular meshes and how to estimate normal vectors and curvatures on the triangular meshes. Without loss of generality, we denote $\mathcal{S} \in \mathbb{R}^3$ as a compact closed triangulation surface of arbitrary topology with no degenerate triangles. The set of vertices, edges and triangles of $\mathcal{S}$ are denoted as $\{\boldsymbol{x}_i : i = 0, 1, \ldots, N-1\}$, $\{\boldsymbol{e}_{i,j} : 0 \le i, j \le M-1\}$ and $\{\tau_i : i = 0, 1, \ldots, T-1\}$, respectively, where N, M and T are the numbers of vertices, edges and triangles, respectively. We introduce the symbol $\prec$ to represent the composition relation, e.g., $\boldsymbol{x} \prec e$ denotes $\boldsymbol{x}$ is an endpoint of an edge e, $e \prec \tau$ denotes e is an edge of a triangle τ, and $\boldsymbol{x} \prec \tau$ denotes $\boldsymbol{x}$ is a vertex of a triangle τ. Let $\mathcal{N}(\boldsymbol{x}_i)$ be the 1-ring of the vertex $\boldsymbol{x}_i$, that is the set of triangles containing $\boldsymbol{x}_i$. Similarly, $\mathcal{N}(e_{i,j})$ denotes the set of triangles containing $e_{i,j}$. Suppose $\{n_i : i = 0, 1, \ldots, N-1\}$ represents the number of triangles containing $\boldsymbol{x}_i$, which is also the total number of adjacent vertices of $\boldsymbol{x}_i$.

There are many methods available to estimate the normals and curvatures on the triangular meshes. The straightforward way to compute the normal vector on each vertex is the weighted average of the normals of its surrounding triangular elements. Suppose we use the equal weights for all triangular as [35], we have the following formula for the *normal*

$$\boldsymbol{N}_i = \frac{1}{n_i} \sum_{\substack{\tau \in \mathcal{N}(\boldsymbol{x}_i), \\ \boldsymbol{x}_i, \boldsymbol{x}_j, \boldsymbol{x}_k \prec \tau}} \frac{(\boldsymbol{x}_i - \boldsymbol{x}_j) \bigotimes (\boldsymbol{x}_i - \boldsymbol{x}_k)}{\|(\boldsymbol{x}_i - \boldsymbol{x}_j) \bigotimes (\boldsymbol{x}_i - \boldsymbol{x}_k)\|}, \tag{1}$$

where $\bigotimes$ denotes the cross product.

We use the mean curvature to describe the degree of deformation for soft objects. Desbrun *et al.* [36] presented the

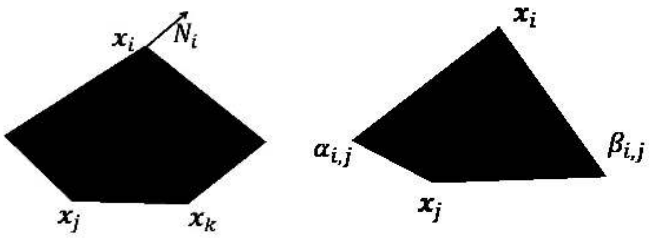

(a) (b)

Fig. 2. Illustration of topological structure of triangular meshes: (a) the 1-ring neighborhood of vertex $\boldsymbol{x}_i$; (b) the locations of α and β, where N_i denotes the averaged normal at mass $\boldsymbol{x}_i$.

curvature normal $\kappa_i \boldsymbol{N}_i$ used to calculate the mean curvature for the point cloud data

$$\kappa_i \boldsymbol{N}_i = \frac{1}{4A} \sum_{\boldsymbol{x}_j \prec \boldsymbol{\tau} \in \mathcal{N}(x_i)} (\cot \alpha_{i,j} + \cot \beta_{i,j})(\boldsymbol{x}_i - \boldsymbol{x}_j), \quad (2)$$

where A is the total area of all triangular patches in the neighborhood of mass point $\boldsymbol{x}_i$, $\alpha_{i,j}$ and $\beta_{i,j}$ are the two opposite angles of the edge $e_{i,j}$ with $\boldsymbol{x}_i$ and $\boldsymbol{x}_j$ as the endpoints, and κ_i denotes the curvature at $\boldsymbol{x}_i$. We provide the 1-ring neighborhood of the vertex $\boldsymbol{x}_i$ and explain the the relation of $\alpha_{i,j}$ and $\beta_{i,j}$ in Fig. 2 (a) and (b), respectively.

B. Our nonlinear mass-spring model

The MSM discretizes the complex shapes into a set of point masses and a set of massless springs connecting the point masses. Suppose our MSM is composed of N point masses and M massless springs. For each mass point $\boldsymbol{x}_i \in \mathbb{R}^3$, $i = 0, 1, \ldots, N-1$, the mass-spring model can be described by Newton's second law as follows

$$\mu_i \boldsymbol{a}_i = \boldsymbol{f}_i, \quad (3)$$

where $\mu_i \in \mathbb{R}$ denotes the mass at $\boldsymbol{x}_i$, $\boldsymbol{a}_i \in \mathbb{R}^3$ denotes the acceleration of mass point $\boldsymbol{x}_i$, and $\boldsymbol{f}_i$ is the total force acting to the mass $\boldsymbol{x}_i$ including both external forces and internal forces.

C. Forces

The force $\boldsymbol{f}$ in the mass-spring system (3) is the total force acting on the point masses, which is the sum of the external forces, spring forces, and damping forces.

1) External forces: The external forces of the system include both the gravity force and man-made forces, where the man-made forces are applied to selected vertices by the force feedback device. Another popular way is to use the position-based approach, which is displacement driven by moving the selected vertices to target positions in an iterative process. The gravity force is acting on every point mass in the system defined by

$$\boldsymbol{f}_i^g = \mu_i \boldsymbol{g}, \quad (4)$$

where $\boldsymbol{g} = [0, 0, -9.8]\ N/kg$ is the gravitational acceleration.

2) Spring forces: Traditionally, the spring force is defined by Hooke's Law, where the strain and stress is constitutive relations of linear elasticity. That is, the force acting on $\boldsymbol{x}_i$ generated by the spring connecting $\boldsymbol{x}_i$ and $\boldsymbol{x}_j$ is in direct proportion to the extension of the spring. Thus, the deformation is linearly related to the magnitude of the forces, which causes the hyper-elasticity effect for large stresses. It appears that the shape deforms significantly for the vertices under stress, while other vertices almost remain unchanged.

While the deformation happens not only for spring elongation and compression but also bending, we introduce Euler's elastica [37] to model the spring deformation. It was first proposed by the mathematician Leonhard Euler for describing the nonlinear constitutive law of the elastic strings, where the elastica means the shape of the ideal thin elastic rod on a plane. The study proclaims the energetic preference of bending over straining a thin elastic rod, and then makes Euler's elastica to be an important concept of continuum mechanics [38]. In light of its continuum mechanical property, we introduce the elastica spring in the three dimensional space to model the nonlinear stress-strain relation. In particular, the elastica spring length is defined as

$$\ell_{i,j}^e = \big(a + b|\kappa_{i,j}|^p\big)\ell_{i,j}, \quad (5)$$

where $\kappa_{i,j}$ denotes the curvature of the spring between $\boldsymbol{x}_i$ and $\boldsymbol{x}_j$, a and b are two positive constant weights, and p is the power of the curvature chosen as $p = 1$ or $p = 2$. As shown both spring length and curvature contribute to soft tissue deformation. And the elastica spring length can degenerate to the original spring length, when no bending happens, i.e., $\kappa = 0$. Then, it is straightforward to define the spring force based on the elatica spring length as follows

$$\boldsymbol{f}_i^s = k_{i,j}(\ell_{i,j}^e - \ell_{i,j}^0) \cdot \frac{\boldsymbol{x}_j - \boldsymbol{x}_i}{|\boldsymbol{x}_j - \boldsymbol{x}_i|}, \quad (6)$$

where $k_{i,j}$ is the spring stiffness, and $\ell_{i,j}^0$ and $\ell_{i,j}^e$ denote the rest length and deformed length of the spring, respectively, and the curvature of the spring $\kappa_{i,j}$ is estimated by averaging the curvatures of the two endpoints with κ_i and κ_j being calculated by the curvature normal (2). Since the spring force becomes a nonlinear function of the length $|\boldsymbol{x}_j - \boldsymbol{x}_i|$, the spring force can reflect the intrinsic nonlinear stress-strain relation of soft tissues. Another important merit of the elastica springs is that the deformation can be more easily transferred from vertices of large curvatures to vertices of small curvatures. Thus, realistic deformation can be obtained with smoother and plumper surfaces during simulation, which is also verified by numerical experiments.

3) Damping forces: Considering the imperfect elasticity of physical bodies, energy dissipation occurs during the deformation. Because the damping force also damps out rotations quickly, it can be defined with the length of the springs as follows

$$\boldsymbol{f}_i^d = d_{i,j} \frac{(\boldsymbol{v}_j - \boldsymbol{v}_i) \cdot (\boldsymbol{x}_j - \boldsymbol{x}_i)}{|\boldsymbol{x}_j - \boldsymbol{x}_i|} \cdot \frac{\boldsymbol{x}_j - \boldsymbol{x}_i}{|\boldsymbol{x}_j - \boldsymbol{x}_i|}, \quad (7)$$

where $d_{i,j}$ denotes the spring damping constant.

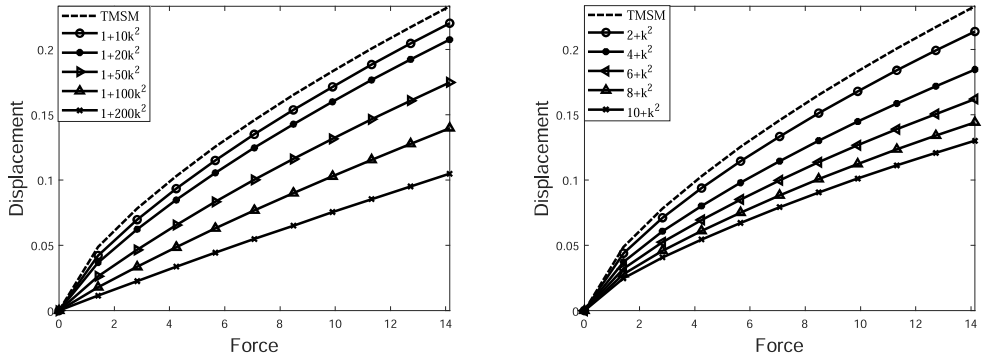

(a) a increases from $a = 2$ to $a = 10$ (b) b increases from $b = 10$ to $b = 200$

Fig. 3. The force-displacement curves of our NMSM, where the x-axis represents the magnitude of the external forces and y-axis represents the displacements.

TABLE I
THE PERFORMANCE COMPARISON WITH RESPECT TO DIFFERENT FORCE, WHERE FORCES ARE TIMED BY $\times$1E-3N.

External force		[1 0 0]	[1 1 0]	[1 1 1]
TMSM	Volume change (%)	-2.56	-3.61	-5.81
	CPU time (s)	0.416	0.681	0.615
	Feedback force	[0.99 0.00 0.03]	[0.99 1.00 -0.02]	[0.99 1.01 0.98]
CMSM	Volume change (%)	-2.00	-3.25	-3.85
	CPU time (s)	4.390	4.902	6.085
	Feedback force	[0.97 0.00 0.00]	[0.97 1.01 0.00]	[1.01 1.00 1.05]
NMSM	Volume change (%)	**-1.84**	**-2.72**	**-3.41**
	CPU Time (s)	2.127	2.954	2.486
	Feedback force	[1.00 0.00 0.00]	[1.00 1.00 -0.02]	[0.98 1.01 0.98]

D. Our algorithm

Similar to [22], we implement the Verlet integration scheme to solve the proposed Nonlinear Mass-Spring Model (NMSM) as summarized in Algorithm 1. Although external forces are used in the algorithm, the position-based attachment can be also applied to obtain the stable interaction between the instrument and virtual organs, which will be demonstrated in Sect. III.

Algorithm 1 The Verlet integration for the proposed NMSM

Initialization: $\boldsymbol{x}_i$, $\boldsymbol{v}_i$, $\boldsymbol{f}_i^d$, $\boldsymbol{f}_i^s$, μ_i, for $i = 0, \cdots, N-1$;
loop
  do
    Obtain the external forces $\boldsymbol{f}_i^e$ from the instrument;
    Compute the gravity $\boldsymbol{f}_i^g$ from (4);
    Compute the spring forces $\boldsymbol{f}_i^s$ from (6);
    Compute the damping forces $\boldsymbol{f}_i^d$ from (7);
    Estimate the resultant forces $\boldsymbol{f}_i \leftarrow \boldsymbol{f}_i^e + \boldsymbol{f}_i^g + \boldsymbol{f}_i^s + \boldsymbol{f}_i^d$;
    Compute the position $\boldsymbol{p}_i \leftarrow \boldsymbol{x}_i + \boldsymbol{v}_i \Delta t + \boldsymbol{f}_i \Delta t^2 / \mu_i$;
    Compute the velocity $\boldsymbol{v}_i \leftarrow (\boldsymbol{p}_i - \boldsymbol{x}_i)/\Delta t$;
  end
  Update the final position for all vertices: $\boldsymbol{x}_i \leftarrow \boldsymbol{p}_i$;
endloop

Remark 1: Note that the proposed algorithm is applicable to integrate with both artificial springs and constraints on point masses and springs such as the previous works [22], [29]–[31].

III. NUMERICAL VALIDATIONS

In the section, we implement the proposed method in C++ and use the OpenGL rendering system on a Dell Desktop with i7-7700 CPU at 3.6GHz. To evaluate the performance of the proposed NMSM, we carry out a series of experiments and compare the results with the traditional mass-spring model (TMSM) and the constrained mass-spring model (CMSM) [22]. There are two model parameters in the CMSM used to control the deformation of the springs, i.e., the stretch ratio τ_s and compression ratio τ_c, where τ_s is chosen in between $\tau_s \in [0, 0.01]$ and τ_c is fixed as $\tau_c = 0.01$ as suggested by [22]. The power of the curvature in (5) is set as $p = 2$ for the spherical mesh and $p = 1$ for the liver meshes. All methods are terminated when either the iteration number reaches 20,000 or the sum of all vertex accelerations is smaller than the tolerance 1×10^{-6}.

A. Model Initialization

Firstly, we explain how to set up the parameters for the triangular mesh models.

1) Point Masses: We assume that the masses are uniformly distributed over the triangular mesh. According to [39], we estimate the mass μ_i, $i = 0, \ldots, N-1$, by the area-weighted average as follows

$$\mu_i = \mu \sum_{\forall \tau_j \in \mathcal{N}(\boldsymbol{x}_i)} \frac{A_j}{3A}, \tag{8}$$

where μ is the total mass of the soft tissue, $\mathcal{N}(\boldsymbol{x}_i)$ is the set of triangular patches containing the vertex $\boldsymbol{x}_i$, A_j is the area of

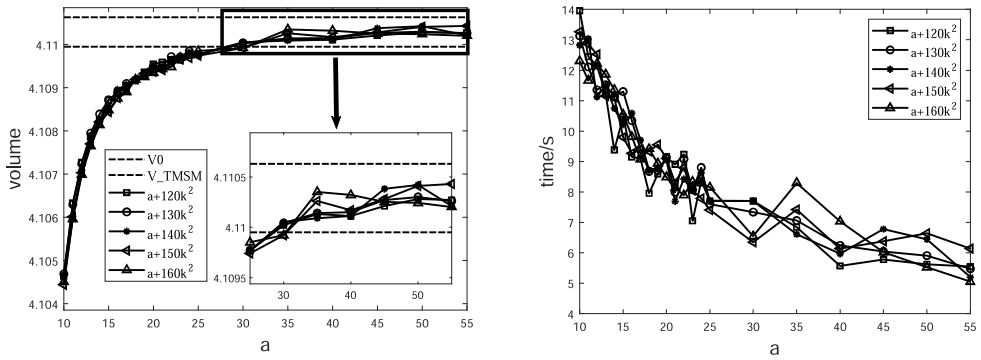

(a) Deformed volume (b) Time consumption

Fig. 4. The comparison of volume deformation and time consumption with respect to different values of a.

the triangular face τ_j and A is the total area of all triangular faces.

2) Spring Stiffness: The spring stiffness describes the stress-strain relation of the soft tissues to a certain degree. Lloyd *et al.* [40] proposed the calculation formula of the spring stiffness based on anisotropic elastic material with Young's modulus and the triangular mesh model. Accordingly, we use the following formula to identify the spring stiffness

$$k_{i,j} = Et \sum_{\forall \tau_j \in \mathcal{N}(e_{i,j})} \frac{\sqrt{3}}{4} \frac{A_j}{A_0}, \tag{9}$$

where t is the thickness of the plane stress elastic model, $\mathcal{N}(e_{i,j})$ is the set of triangular faces containing the edge $e_{i,j}$, and A_0 is the area of an equilateral triangle with edge length $e_{i,j}$. Note that we set the thickness $t = 10^{-3}$ m for liver experiments.

3) Spring Damping: According to [41], we define the damping stiffness to guarantee the best behavior consistency for different and combined resolutions, which gives

$$d_{i,j} = 2\frac{\sqrt{k_{i,j}(\mu_i + \mu_j)}}{l^0_{i,j}}. \tag{10}$$

4) Behaviors of the elastica springs: There are two important parameters a and b for the elastica spring length (5), which can depict the physical properties of soft tissues. Thus, we carry out a series of experiments on a dimensionless spherical mesh with a radius of 1 and point-wise mass of 1. Note that the mesh is composed of 162 vertices and 320 faces with uniform springs of spring coefficient $k = 30$ and damping coefficient $d = 100$. We perform the tensile tests based on the force-driven method, where the external forces of $\boldsymbol{f}^e = [0, 1, 1]$ to $\boldsymbol{f}^e = [0, 10, 10]$ are applied to the same vertices on the sphere. To identify the influences of a and b, we first fix the value of b and increase a gradually, and vice versa. The force-displacement curves using the averaged displacements of all vertices with different combinations of a and b are displayed in Fig. 3, where the dashed red line denotes the traditional mass-spring model. For the fixed b, the nonlinearity becomes weaker and weaker as the value of a increases. On the other hand, the nonlinearity becomes stronger and stronger as the value of b increases.

Our NMSM can also help to preserve the volume during the simulation process. We apply an external force of $\boldsymbol{f}^e = [0, 4, 4]$ to the same spherical mesh, where b is chosen from $b \in \{120, 130, 140, 150, 160\}$ and a is increased from 10 to 55 with the step size of 5. We track the deformed volumes and plot them in Fig. 4 (a), where all curves are of the same trend. When $a < 30$, the deformed volume is smaller than the original volume (marked by the dashed red line). As a keeps increasing, the deformed volume becomes stable, which is smaller than the deformed volume obtained by the TMSM (marked by the dashed blue line). On the other hand, we record the computational time of our NMSM in Fig. 4 (b), where less time is consumed as a increasing from 10 to 55. Because the nonlinearity can be controlled by either a or b, we simply set $a = 1$ and tune b to control the deformation in the following experiments.

B. Measurement of feedback forces

Realistic anatomical virtual reality needs accurate haptic feedback to ensure the users can experience the biomechanical properties of tissues and organs. Thus, we perform a stress-relaxation test on a human liver model with a size of 170 mm $\times$ 140 mm $\times$ 160 mm, which contains 1000 faces and 502 vertices. More specifically, we apply different external forces on the top surface of the liver model and examine the volume change, CPU time, and feedback forces obtained by TMSM, CMSM, and our NMSM. As shown in Table I, our NMSM can provide more accurate feedback forces than TMSM and CMSM when the liver model is tensing the same external forces. Simultaneously, the volume change of our model is also the smallest, which demonstrates its advantages for modeling incompressible soft tissues.

C. Experiments on the liver model

We also implement our NMSM by the position-based attachment, which is a popular strategy used in virtual reality. For a more in-depth comparison, we generate two liver mesh models to represent the liver, one of 1000 faces and the other one of 2000 faces. Two different displacements are applied to the same selected face, which is denoted as the small

TABLE II
THE COMPARISON BETWEEN THE TMSM, CMSM AND OUR NMSM IN TERMS OF VOLUME CHANGE (VC) AND TIME CONSUMPTION ON THE LIVER DEFORMATION.

	Small displacement						Large displacement					
No. of face	1000 faces			2000 faces			1000 faces			2000 faces		
Method	TMSM	CMSM	NMSM	TMSM	CMSM	NMSM	TMSM	CMSM	NMSM	TMSM	CMSM	NMSM
VC (%)	0.68	**0.37**	0.45	0.72	0.66	**0.60**	1.24	**0.91**	1.11	1.23	1.3	**1.01**
Time (s)	**0.002**	0.01	0.003	**0.007**	0.019	0.008	**0.002**	0.011	0.004	**0.007**	0.019	0.008

TABLE III
THE PERFORMANCE COMPARISON BETWEEN OUR NMSM AND CMSM IN TERMS OF TIME COSTS AND CHANGES OF VOLUME WITH RESPECT TO DIFFERENT MESH MODELS.

No. of faces	2000	4000	6000	8000	10000
Parameter b	0.3	0.2	0.15	0.15	0.15
NMSM volume change (%)	**0.73**	**0.60**	**0.56**	**0.49**	**0.39**
CMSM volume change (%)	0.84	0.72	0.66	0.57	0.48
NMSM CPU time (s)	**0.009**	**0.019**	**0.028**	**0.037**	**0.047**
CMSM CPU time (s)	0.011	0.023	0.034	0.046	0.056

displacement and large displacement, respectively. The small-displacement moves the selected triangular face by a distance of [0,20,20] mm, while the large displacement moves the same triangular face by a distance of [0,30,30] mm. In the experiments, we set $b = 0.5$ and $b = 0.2$ for the mesh model with 1000 faces and 2000 faces, respectively, where a larger b is used for the sparser model to preserve the volume. For the same purpose, we set $\tau_s = 0$ for the CMSM. Besides, we fix the number of iteration to be 30 for the TMSM, CMSM, and NMSM for a fair comparison. Table II exhibits both volume change and computational time of the three models for different combinations of the mesh models and deformations. As can be observed, our NMSM performs the best in balancing the volume preservation and efficiency among the three mass-spring methods. To be specific, we have the following conclusions

- The volume change increases when either the displacement becomes larger or the mesh model becomes sparser for all methods. For the fixed mesh model and displacement, our NMSM always results in a smaller volume change than the TMSM, which is an important property for the incompressible soft tissue simulation such as the liver.
- The time consumption is affected by the size of the mesh model such that the denser mesh model requires more CPU time to deform. Because of the low computational costs of the curvature, our NMSM works almost as efficiently as the TMSM, both of which are faster than the CMSM requiring an inner iteration on the spring constraints.

Moreover, we display the results of the small deformation and large deformation in Fig. 5, where similar visual results are obtained by the three mass-spring models.

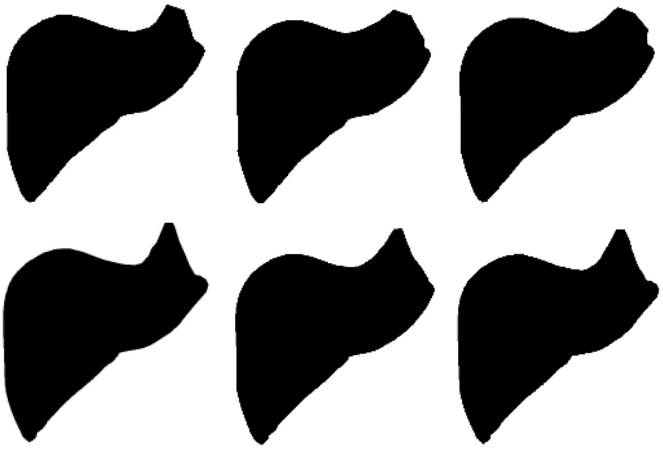

(a) TMSM (b) CMSM (c) NMSM

Fig. 5. The deformation comparison among the TMSM, CMSM and NMSM for both small and large displacements, where pink and red color denote the original and deformed mesh, respectively. The first row and second row correspond to the small and large deformation, respectively.

D. Real-time Interactive Simulation

Our final purpose is to simulate the soft tissue deformation in a real-time virtual reality environment, for which the update rate for the visual feedback is required to be at least 30 Hz to achieve continuous motion of rendered graphics to the human sensory system. In the following, we conduct a series of experiments to demonstrate our NMSM can ensure real-time simulation in virtual reality.

More specifically, we generate five mesh models of different resolutions to represent the liver, which contain 2000 faces, 4000 faces, 6000 faces, 8000 faces, and 10000 faces, respectively. In our mass-spring system, we fix $a = 1$ and choose b in the range $b \in [0.01, 0.5]$ to control the elastic properties of liver models. Normally a large value of b is used for the sparser models to guarantee volume preservation. To obtain the realistic simulation, we introduce the overstretching compensation on the springs with $\tau_s = 0.01$. For a comparative study, we also evaluate the CMSM with both overstretching compensation and over-compressing compensation, where both the stretch ratio and compression ratio are set as $\tau_s = \tau_c = 0.01$. The value of b, the average changes of volume, and the average CPU time costs are listed in Table III. When increasing the

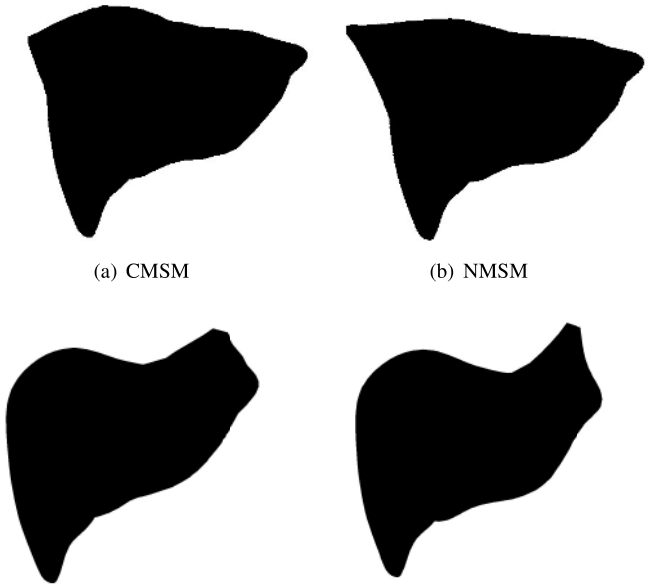

(a) CMSM (b) NMSM

(c) CMSM (d) NMSM

Fig. 6. The real-time manipulations of the liver in the virtual reality environment, where (a), (c) are obtained by CMSM and (b), (d) are obtained by NMSM.

number of faces, the change of volume for both NMSM and CMSM becomes smaller and smaller by sacrificing efficiency. Our NMSM always gives better simulation results than CMSM in both efficiency and volume preservation.

Moreover, we display two scenarios of the deformation sequence from the virtual reality environment obtained by the mesh model with 4000 faces in Fig. 6, where the position-based attachment is used to accurately control the soft tissue with the selected triangular face marked by red color. Although the CMSM works well on the tetrahedral mesh models, its performance on triangular meshes is unsatisfactory, the deformation of which is unrealistic with bumpy surfaces. Thanks to the elastica springs, our NMSM produces better simulation results with smoother and plumper surfaces.

IV. Anatomical virtual reality

The virtual reality and 3D visualization system can help to make the learning process more efficient and enjoyable, and less time consuming, which works as a good candidate to replace the traditional pedagogic methods [42], [43]. However, the current anatomical virtual realities have limited capability to model the biomechanical properties of organs and tissues. Thus, cadavers remain a major component of teaching [44]. In this section, we develop an interactive anatomical virtual reality to provide an immersive environment allied with the biomechanical properties of soft tissues. As shown in Fig. 7, our system involves four main steps as listed below

Step 1: We first use the grow-from-seeds method provided in 3D Slicer image computing platform [45] to realize organ segmentation, where most organs of the thoracic and abdominal cavity are involved including heart, lung, liver, gallbladder, stomach, spleen, kidneys, pancreas and diaphragm.

TABLE IV
The mesh models used in our anatomical virtual reality environment.

Mesh models	No. of vertices	No. of faces
Heart	502	1000
Lung	1502	3000
Artery	752	1500
Diaphragm	502	1000
Liver	2502	5000
Gallbladder	252	500
Stomach	502	1000
Spleen	502	1000
Pancreas	402	800
Left kidney	402	800
Right kidney	402	800
in total	8222	16400

Step 2: We then generate the triangular mesh models for all organs and tissues in MeshLab to balance the geometric accuracy and computational burden for deformation simulation. The physiological connection between different organs is also introduced according to anthropotomy, which can be realized by enforcing the boundary conditions in between organs and tissues such as the liver and gallbladder, liver and diaphragm, etc.

Step 3: We equip the multi-organ system with our NMSM as the physical engine, which can provide real-time and realistic simulation subjected to external forces.

Step 4: Lastly, we realize the human-computer interaction using the haptic device, which can produce true-to-life touch sensations as the users manipulate on-screen 3D organs.

Note that we segment both heart atrium and ventricles as illustrated in Fig. 8 (a), but the cardiac vesicle model is used in our conceptual virtual reality system. In what follows, the triangular mesh models are generated for each organ, the numbers of vertices and faces of which are displayed in Table IV. As illustrated in Fig. 9, the abdominal organs are supported by the peritoneum in three different ways, including the extra-peritoneal organs (e.g., kidney, pancreas, etc), inter-peritoneal organs (e.g., liver, etc), and endo-peritoneal organs (e.g., stomach, spleen, etc). Thus, we introduce springs in between the connected organs such as liver and diaphragm, liver and gallbladder, stomach and diaphragm, and stomach and spleen in our virtual reality environment. Please refer to Fig. 8 (b) and (c) for the illustration of the location between liver and diaphragm, and the connection springs between liver and gallbladder, respectively.

In the simulation, the parameters of our model are set as $a = 1$ and $b = 0.1$ for all organ models and the over-stretching constraint is applied to springs with $\tau_s = 0.01$. We select four typical interactive scenarios and display them in Fig. 10 including pulling the left lung, right lung, and liver. Note that the diaphragm, which performs as the boundary condition for the liver and stomach, is rendered to be transparent for better visual effect. More importantly, our multi-organ deformable system takes around 33 ms during the interaction, which offers a real-time 3D representation of human coelom in an interactive virtual reality environment.

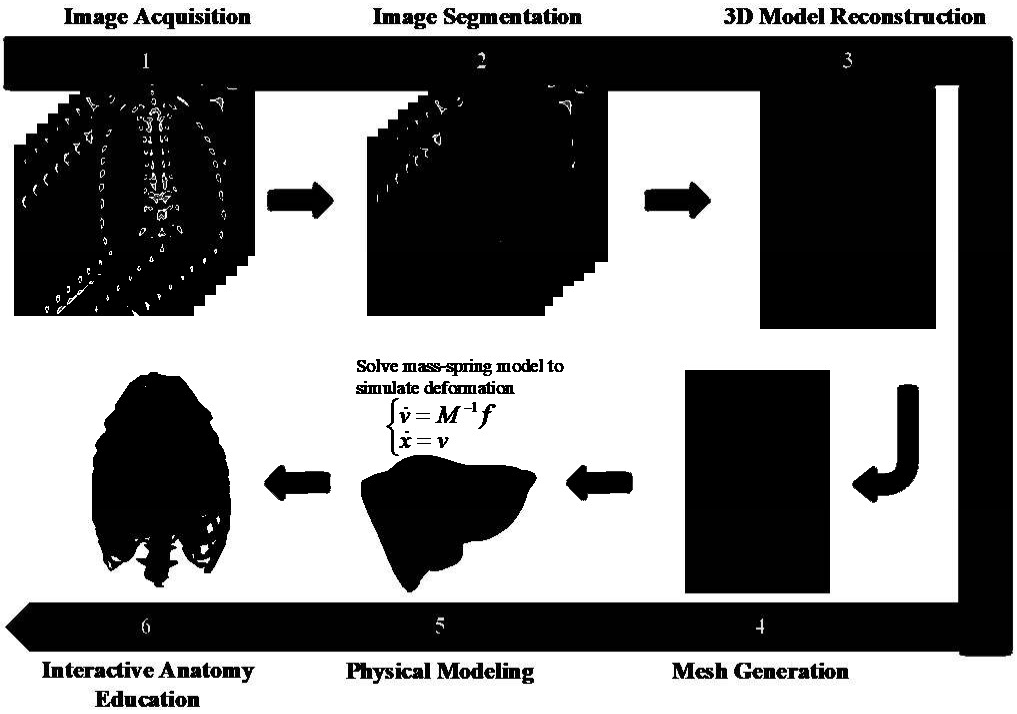

Fig. 7. Schematic drawings for the procedures of an interactive virtual reality system for anatomy education, including 1) acquisition of CT images; 2) segmentation of the organs and tissues; 3) reconstruction of 3D models; 4) mesh generation to discretize the 3D models; 5) solve Newton's second law to simulate the deformation; 6) presentation of simulations.

(a) heart (b) liver and diaphragm (c) liver and gallbladder

Fig. 8. Illustration of the heart segmentation, the location of the diaphragm, and the connection springs in between liver and gallbladder. In the figure, red lines denote the connected springs and black lines denote the body springs.

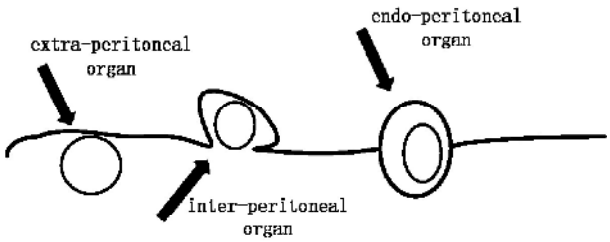

Fig. 9. The connection relationships between the abdominal organs and peritoneum.

V. Discussion and Concluding Remarks

To equip the organs in an anatomical virtual reality with mechanical properties, it requires an efficient simulator to well balance deformation accuracy and real-time computation. Compared to the traditional MSM and constrained MSM for soft tissue deformation, the proposed NMSM is more suitable for triangular mesh models, significantly improving the computational efficiency and the simulation accuracy. In particular, it has the following characteristics and advantages: (1) The elastica springs are introduced to model the nonlinear stress-strain relation of soft tissues, where both length deformation and bending deformation are naturally combined and used to measure the spring forces. (2) The computational burden resulting from the elastica spring length is very low, only requiring a few simple algebraic operations over the point masses, which is also verified by the time compared with the TMSM and CMSM. (3) The elastica springs can be applied to most existing mass-spring models to provide realistic simulation.

On the other hand, the proposed NMSM and anatomical virtual reality also have some limitations that should be investigated in our future works. (1) The parameters involved in our NMSM are also important to the performance. Currently, we use empirical formula (8), (9) and (10) to estimate the point masses, spring stiffness and spring damping for soft tissues. The link between these parameters to the material parameters such as Young's modulus and Poisson's ratio should be established to guarantee accurate simulation. Although the two parameters a and b in the elastica spring length (5) can be chosen manually based on performance, it is better to construct a law to compute them according to the mechanical behavior of soft tissues. (2) The proposed anatomical virtual reality is a prototype missing necessary functional components such as the collision detection between organs, virtual tool model, etc.

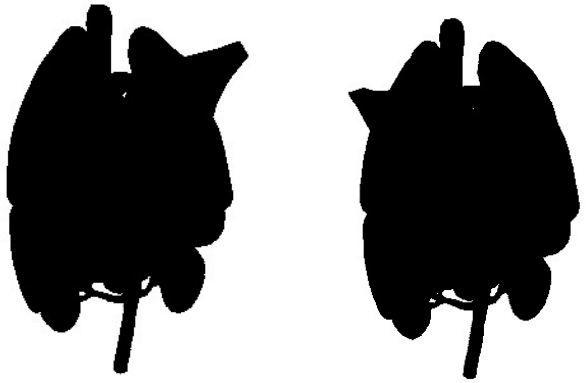

(a) pull the left lung (b) pull the right lung

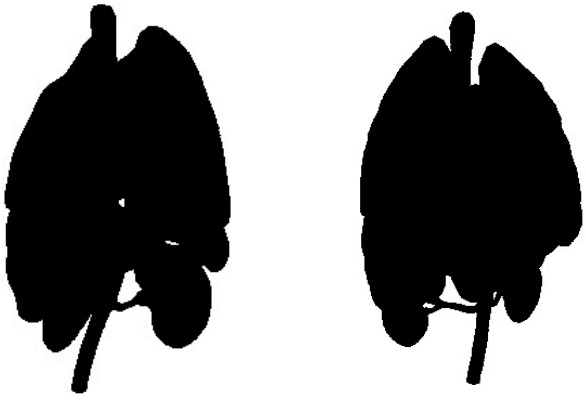

(c) rotate and pull the lung (d) rotate and pull the liver

Fig. 10. Selective scenarios obtained in our anatomical virtual reality system, where lung, heart, diaphragm, liver, gallbladder, stomach, spleen, pancreas, and kidney are exhibited in the system.

(3) Considering the future application of the proposed NMSM on complicated mesh models, the GPU-based implementation of the proposed model is necessary to further improve the computational efficiency.

In conclusion, we have developed an accurate and efficient nonlinear mass-spring model for a visuo-haptic surgical simulator, where the elastica springs were introduced to mimic the biomechanical properties of soft tissues. Our model is an ideal choice for the triangular surface meshes, which can not only simulate the soft tissue with smoother surfaces but also measure the nonlinear behaviors such as viscoelasticity and incompressibility. Taking the human liver as an example, both position-based and force-based interactions were implemented in our model making it easy to be integrated with the haptic instrument. We further developed a visuo-haptic simulator for anatomical education with the proposed model as the physical engine, which shows its high computational efficiency. We believe the proposed nonlinear mass-spring model can have broad applications for various visuo-haptic scenarios such as surgical simulation, training, and planning, etc.

REFERENCES

[1] H. Huo, X. Liu, Z. Wu, Z. Tang, M. Tang, D. Chen, Y. Dong, X. Qiao, T. Liu, R. An, and Y. Fan, "Design of robot-assisted task involving visuomotor conflict for identification of proprioceptive acuity," *IEEE Transactions on Instrumentation and Measurement*, vol. 70, pp. 1–10, 2021.

[2] R. M. Viglialoro, N. Esposito, S. Condino, F. Cutolo, S. Guadagni, M. Gesi, M. Ferrari, and V. Ferrari, "Augmented reality to improve surgical simulation: Lessons learned towards the design of a hybrid laparoscopic simulator for cholecystectomy," *IEEE Transactions on Biomedical Engineering*, vol. 66, no. 7, pp. 2091–2104, Jul. 2019.

[3] S. Guo, X. Cai, and B. Gao, "A tensor-mass method-based vascular model and its performance evaluation for interventional surgery virtual reality simulator," *The International Journal of Medical Robotics and Computer Assisted Surgery*, vol. 14, no. 6, p. e1946, Aug. 2018.

[4] G. Caccianiga, A. Mariani, C. G. de Paratesi, A. Menciassi, and E. D. Momi, "Multi-sensory guidance and feedback for simulation-based training in robot assisted surgery: A preliminary comparison of visual, haptic, and visuo-haptic," *IEEE Robotics and Automation Letters*, vol. 6, no. 2, pp. 3801–3808, Apr. 2021.

[5] S. Li, J. Cui, A. Hao, S. Zhang, and Q. Zhao, "Design and evaluation of personalized percutaneous coronary intervention surgery simulation system," *IEEE Transactions on Visualization and Computer Graphics*, vol. 27, no. 11, pp. 4150–4160, Nov. 2021.

[6] D. Wang, C. Yang, Y. Zhang, and J. Xiao, "Toward in-vivo force and motion measurement for vascular surgery," *IEEE Transactions on Instrumentation and Measurement*, vol. 63, no. 8, pp. 1975–1982, Aug. 2014.

[7] M. Wei, Y. Liu, H. Dong, and A. E. Saddik, "Human head stiffness rendering," *IEEE Transactions on Instrumentation and Measurement*, vol. 66, no. 8, pp. 2083–2096, Aug. 2017.

[8] W. Shi, P. X. Liu, and M. Zheng, "Bleeding simulation with improved visual effects for surgical simulation systems," *IEEE Transactions on Systems, Man, and Cybernetics: Systems*, vol. 51, no. 2, pp. 686–695, Feb. 2021.

[9] K. Barbe, C. Ford, K. Bonn, and J. Gilbert, "Toward a tissue model for bipolar electrosurgery: Block-oriented model structure analysis," *IEEE Transactions on Instrumentation and Measurement*, vol. 66, no. 3, pp. 460–469, Mar. 2017.

[10] A. Segato, C. D. Vece, S. Zucchelli, M. D. Marzo, T. Wendler, M. F. Azampour, S. Galvan, R. Secoli, and E. D. Momi, "Position-based dynamics simulator of brain deformations for path planning and intra-operative control in keyhole neurosurgery," *IEEE Robotics and Automation Letters*, vol. 6, no. 3, pp. 6061–6067, Jul. 2021.

[11] Y. I. Kim, S.-Y. Jung, S. Min, E. Seol, S. Seo, J.-W. Hur, D. Jung, H.-J. Lee, S. Lee, G. J. Kim, C.-Y. Cho, S. Choi, S.-M. Lee, and C.-H. Cho, "Visuo-haptic-based multimodal feedback virtual reality solution to improve anxiety symptoms: A proof-of-concept study," *Psychiatry Investigation*, vol. 16, no. 2, pp. 167–171, Feb. 2019.

[12] P. Arpaia, L. Duraccio, N. Moccaldi, and S. Rossi, "Wearable brain–computer interface instrumentation for robot-based rehabilitation by augmented reality," *IEEE Transactions on Instrumentation and Measurement*, vol. 69, no. 9, pp. 6362–6371, Sep. 2020.

[13] J. Li, Z. Wang, S. Qiu, H. Zhao, Q. Wang, D. Plettemeier, B. Liang, and X. Shi, "Using body sensor network to measure the effect of rehabilitation therapy on improvement of lower limb motor function in children with spastic diplegia," *IEEE Transactions on Instrumentation and Measurement*, vol. 69, no. 11, pp. 9215–9227, Nov. 2020.

[14] N. Baghaei, V. Chitale, A. Hlasnik, L. Stemmet, H.-N. Liang, and R. Porter, "Virtual reality for supporting the treatment of depression and anxiety: Scoping review," *JMIR Mental Health*, vol. 8, no. 9, p. e29681, Sep. 2021.

[15] X. P. Liu, S. Xu, H. Zhang, and L. Hu, "A new hybrid soft tissue model for visio-haptic simulation," *IEEE Transactions on Instrumentation and Measurement*, vol. 60, no. 11, pp. 3570–3581, Nov. 2011.

[16] Y. Zou, P. X. Liu, Q. Cheng, P. Lai, and C. Li, "A new deformation model of biological tissue for surgery simulation," *IEEE Transactions on Cybernetics*, vol. 47, no. 11, pp. 3494–3503, Nov. 2017.

[17] W. Hou, P. X. Liu, M. Zheng, and S. Liu, "A new deformation model of brain tissues for neurosurgical simulation," *IEEE Transactions on Instrumentation and Measurement*, vol. 69, no. 4, pp. 1251–1258, Apr. 2020.

[18] J. Zhang, Y. Zhong, and C. Gu, "Deformable models for surgical simulation: A survey," *IEEE Reviews in Biomedical Engineering*, vol. 11, pp. 143–164, 2018.

[19] M. Bro-Nielsen and S. Cotin, "Real-time volumetric deformable models for surgery simulation using finite elements and condensation," *Computer Graphics Forum*, vol. 15, no. 3, pp. 57–66, 1996.

[20] I. Peterlík, H. Courtecuisse, R. Rohling, P. Abolmaesumi, C. Nguan, S. Cotin, and S. Salcudean, "Fast elastic registration of soft tissues under

large deformations," *Medical Image Analysis*, vol. 45, pp. 24–40, Apr. 2018.

[21] P. E. Hammer, M. S. Sacks, P. J. del Nido, and R. D. Howe, "Mass-spring model for simulation of heart valve tissue mechanical behavior," *Annals of Biomedical Engineering*, vol. 39, no. 6, pp. 1668–1679, Feb. 2011.

[22] Y. Duan, W. Huang, H. Chang, W. Chen, J. Zhou, S. K. Teo, Y. Su, C. K. Chui, and S. Chang, "Volume preserved mass–spring model with novel constraints for soft tissue deformation," *IEEE Journal of Biomedical and Health Informatics*, vol. 20, no. 1, pp. 268–280, Jan. 2016.

[23] O. Etzmuss, J. Gross, and W. Strasser, "Deriving a particle system from continuum mechanics for the animation of deformable objects," *IEEE Transactions on Visualization and Computer Graphics*, vol. 9, no. 4, pp. 538–550, 2003.

[24] K. Golec, J.-F. Palierne, F. Zara, S. Nicolle, and G. Damiand, "Hybrid 3d mass-spring system for simulation of isotropic materials with any poisson's ratio," *The Visual Computer*, vol. 36, no. 4, pp. 809–825, May 2019.

[25] G. S. P. Miller, "The motion dynamics of snakes and worms," *ACM SIGGRAPH Computer Graphics*, vol. 22, no. 4, pp. 169–173, Aug. 1988.

[26] S. Cotin, H. Delingette, and N. Ayache, "Real-time elastic deformations of soft tissues for surgery simulation." *IEEE Transactions on Visualization and Computer Graphics*, vol. 5, no. 1, pp. 62–73, 1999.

[27] D. Bourguignon and M.-P. Cani, "Controlling anisotropy in mass-spring systems," in *Eurographics*. Springer Vienna, 2000, pp. 113–123.

[28] W. Mollemans, F. Schutyser, J. V. Cleynenbreugel, and P. Suetens, "Fast soft tissue deformation with tetrahedral mass spring model for maxillofacial surgery planning systems," in *Medical Image Computing and Computer-Assisted Intervention – MICCAI 2004*. Springer Berlin Heidelberg, 2004, pp. 371–379.

[29] L. Nedel and D. Thalmann, "Real time muscle deformations using mass-spring systems," in *Proceedings. Computer Graphics International*. IEEE Comput. Soc, 1998, pp. 156–165.

[30] M. Hong, S. Jung, M.-H. Choi, and S. Welch, "Fast volume preservation for a mass-spring system," *IEEE Computer Graphics and Applications*, vol. 26, no. 5, pp. 83–91, Sep. 2006.

[31] E. Basafa and F. Farahmand, "Real-time simulation of the nonlinear visco-elastic deformations of soft tissues," *International Journal of Computer Assisted Radiology and Surgery*, vol. 6, no. 3, pp. 297–307, Jul. 2011.

[32] S. Xu, X. P. Liu, H. Zhang, and L. Hu, "A nonlinear viscoelastic tensor-mass visual model for surgery simulation," *IEEE Transactions on Instrumentation and Measurement*, vol. 60, no. 1, pp. 14–20, Jan. 2011.

[33] G. San-Vicente, I. Aguinaga, and J. Celigueta, "Cubical mass-spring model design based on a tensile deformation test and nonlinear material model," *IEEE Transactions on Visualization and Computer Graphics*, vol. 18, no. 2, pp. 228–241, 2011.

[34] C. Li, J. Ding, Z. Hong, Y. Pan, and P. X. Liu, "A surface mass-spring model with new flexion springs and collision detection algorithms based on volume structure for real-time soft-tissue deformation interaction," *IEEE Access*, vol. 6, pp. 75 572–75 597, 2018.

[35] H. Gouraud, "Continuous shading of curved surfaces," *IEEE Transactions on Computers*, vol. C-20, no. 6, pp. 623–629, Jun. 1971.

[36] M. Desbrun, M. Meyer, P. Schröder, and A. H. Barr, "Implicit fairing of irregular meshes using diffusion and curvature flow," in *Proceedings of the 26th annual conference on Computer graphics and interactive techniques - SIGGRAPH99*. ACM Press, 1999, pp. 317–324.

[37] R. Levien, "The elastica: a mathematical history (Univ of California, Berkeley)," *Technical report UCB/EECS-2008-103*, 2008.

[38] B. Davidovitch, Y. Sun, and G. M. Grason, "Geometrically incompatible confinement of solids," *Proceedings of the National Academy of Sciences*, vol. 116, no. 5, pp. 1483–1488, Dec. 2018.

[39] G. Wang, B. Wang, Q. Gang, S. Zhou, and X. Liu, "Physical modeling of vascular tissues and stress analysis optimization based on real soft tissue characteristics," in *Proceedings of the 29th International Conference on Computer Animation and Social Agents*, 2016, pp. 29–34.

[40] B. Lloyd, G. Székely, and M. Harders, "Identification of spring parameters for deformable object simulation," *IEEE Transactions on Visualization and Computer Graphics*, vol. 13, no. 5, pp. 1081–1094, 2007.

[41] C. Paloc, F. Bello, R. Kitney, and A. Darzi, "Online multiresolution volumetric mass spring model for real time soft tissue deformation," in *Medical Image Computing and Computer-Assisted Intervention*, 2002, pp. 219–226.

[42] J. W. V. de Faria, M. J. Teixeira, L. de Moura Sousa Júnior, J. P. Otoch, and E. G. Figueiredo, "Virtual and stereoscopic anatomy: when virtual reality meets medical education," *Journal of Neurosurgery*, vol. 125, no. 5, pp. 1105–1111, Nov. 2016.

[43] P. Maniam, P. Schnell, L. Dan, R. Portelli, C. Erolin, R. Mountain, and T. Wilkinson, "Exploration of temporal bone anatomy using mixed reality (HoloLens): development of a mixed reality anatomy teaching resource prototype," *Journal of Visual Communication in Medicine*, vol. 43, no. 1, pp. 17–26, Oct. 2019.

[44] C. Moro, Z. Štromberga, A. Raikos, and A. Stirling, "The effectiveness of virtual and augmented reality in health sciences and medical anatomy," *Anatomical Sciences Education*, vol. 10, no. 6, pp. 549–559, Apr. 2017.

[45] A. Fedorov, R. Beichel, J. Kalpathy-Cramer, J. Finet, J.-C. Fillion-Robin, S. Pujol, C. Bauer, D. Jennings, F. Fennessy, M. Sonka, J. Buatti, S. Aylward, J. V. Miller, S. Pieper, and R. Kikinis, "3d slicer as an image computing platform for the quantitative imaging network," *Magnetic Resonance Imaging*, vol. 30, no. 9, pp. 1323–1341, Nov. 2012.